Bioinspired Synthesis of $Ce_{1-x}O_2$:x%Cu^{2+} Nanobelts for CO Oxidation and Organic Dye Degradation

Yida Huang,[#] Youlong Liang,[#] Chaoran Xie,[#] Qingyuan Gui, Jinlei Ma, Hongxian Pan, Zeyu Tian, Lei Qi,* and Mei Yang*

ACCESS | Metrics & More | Article Recommendations | Supporting Information

ABSTRACT: $Ce_{1-x}O_2$:x%Cu^{2+} nanobelts were bioinspired, designed, and fabricated using commercial filter papers as scaffolds by adding $Cu(NO_3)_2$ in the original sol solution of CeO_2 nanobelts, which display excellent catalyst properties for CO oxidation and photocatalytic activity for organic dyes. Compared with pure CeO_2, CuO belts were synthesized using the same method and the corresponding $Ce_{0.5}O_2$:50%Cu^{2+} bulk materials were synthesized without filter paper as scaffolds; the synthesized $Ce_{1-x}O_2$:x%Cu^{2+} nanobelts, especially $Ce_{0.5}O_2$:50%Cu^{2+} nanobelts, can decrease the reaction temperature of CO to CO_2 at 100 °C with the conversion rate of 100%, much lower than the formerly reported kinds of $Ce_{1-x}O_2$:x%Cu^{2+} catalysts. Meanwhile, the synthesized $Ce_{1-x}O_2$:x%Cu^{2+} nanobelts also display better photocatalytic activity for organic dyes. All of these results provide useful information for the potential applications of the synthesized $Ce_{1-x}O_2$:x%Cu^{2+} nanobelts in catalyst fields.
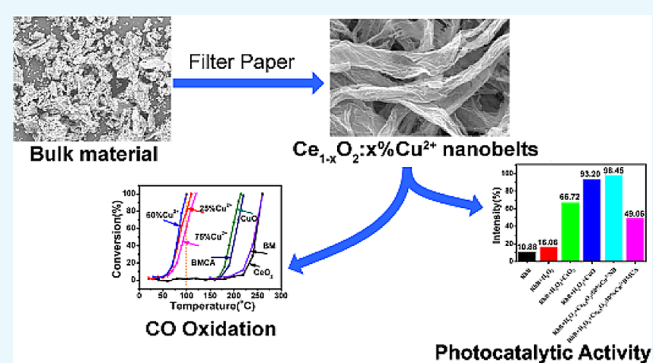
1. INTRODUCTION

Because of the special electronic, optical, and chemical characteristics arising from 4f electrons, CeO_2 nanomaterials have been widely investigated in light of their kinds of applications.[1−3] They have been well recognized as an efficient oxidation catalyst and catalyst support for their high oxygen storage capacity and excellent redox properties arising from their fast switching between the redox couple Ce^{3+}/Ce^{4+}.[4] As a strategy to improve the catalytic performance of CeO_2, incorporation of additional dopants (Zr, Cu, La, Mn, etc.) in the CeO_2 support has been proven to be a good method to enhance the physicochemical and catalytic properties of composites. The thermal stability, redox properties, surface area, and other properties of the composites can be adjusted through changing surface element compositions.[5−9] Meanwhile, the doping of additional metal ions can form oxygen vacancies and other defective structures, which can further improve the oxygen-storage capacity and oxygen anion mobility of the final composites,[10−13] resulting in the striking enhancement of catalytic properties in many reactions, such as water−gas shift reactions, preferential CO oxidation, formaldehyde and methane oxidation, and other reactions.[14−16] Up to now, many kinds of dopants have been cultivated to change the surface element composition with the purpose of promoting the active oxygen content on the CeO_2 surface, which ultimately reveals obviously the high catalytic activity.[5−9,14−16]

As one kind of cultivated ions, Cu^{2+} ions doped in CeO_2 nanocomposites are of great interest in light of their high catalytic activity for CO oxidation because of the special structure complement of CuO and CeO_2.[17−20] The catalytic performance of $Ce_{1-x}O_2$:x%Cu^{2+} composites is much better than those of pure CuO and CeO_2 in some aspects, which include promising application in CO oxidation,[17,18] PROX,[19] SO_2 catalysis,[20] and so on.[21] Compared with the most effective oxidation catalysts to eliminate CO, noble metal (Pd, Pt, and Rh) catalysts,[22] $Ce_{1-x}O_2$:x%Cu^{2+} composites show high activity, low cost, and relatively affluent properties, which makes them an ideal alternative for CO oxidation. Meanwhile, as a low-valence state material, Cu^{2+} ions play an important role in $Ce_{1-x}O_2$:x%Cu^{2+} photocatalysts with their stable oxidation state, inducing the charge compensation and the promotion of oxygen vacancies ($V_o^•$) with the Cu^{2+} impurity phase, leading to higher photocatalytic behavior.[23,24] Meanwhile, the substitution of oxygen vacancies with Ce and Cu states also plays a significant role in the stronger visible catalytic response in the $Ce_{1-x}O_2$:x%Cu^{2+} systems.[25]
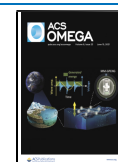
Besides the interactions between CuO and CeO_2, which can strongly affect the catalytic activity of the final composites, the loading amounts and dispersion states of CuO in the CeO_2 matrix can also strikingly influence the interaction between CuO and CeO_2.[26] The catalytic performance of the final composites can be improved dramatically by improving the dispersion of CuO particles.[27,28] However, it is difficult to prepare binary oxides with good dispersion owing to the difference of the phase structures and lattices of CuO and CeO_2. Meanwhile, the tendency of Cu(II) ions to separate from the CeO_2 matrix in the form of nonactive tenorite (CuO) particles makes the loading amount of Cu(II) ions hardly increased in a common procedure to prepare $Ce_{1-x}O_2$:x%Cu^{2+} composites with better properties. Therefore, the choice of the preparation method is very important; to date, various methods have been tried, such as coprecipitation,[26] conventional wet impregnation method and deposition−precipitation method,[27] homogeneous thermal decomposition of urea,[28] flame spray pyrolysis,[29] surfactant-template method, and so on.[17] However, there have been a few literature studies reporting the method using natural cellulosic substances as a scaffold to prepare $Ce_{1-x}O_2$:x%Cu^{2+} composites. As one kind of bioinspired synthetic strategy, it is believed that this kind of synthesis method can introduce some excellent properties of biological organisms into artificial materials, providing diverse functional materials with complex morphologies. Among the kinds of natural substances employed as template substrates, natural cellulose substances possess sophisticated three-dimensional morphological hierarchies, which have been adopted as ideal biotemplates or scaffolds to yield various functional nanomaterials.[30,31]

In this paper, $Ce_{1-x}O_2$:x%Cu^{2+} nanobelt composites were synthesized in a yield of about 68% using commercial filter papers as scaffolds by adding $Cu(NO_3)_2$ into the original sol solution of CeO_2 nanobelts. The scanning electron microscopy (SEM) images indicate that there were no separated CuO particles appearing in the obtained nanobelts when the doping amounts of Cu^{2+} ions were not higher than 50%. The H_2 temperature-programmed reduction (TPR) curves and the catalytic evaluation results indicate that the obtained $Ce_{1-x}O_2$:x%Cu^{2+} complex catalysts have an excellent catalyst effect on CO oxidation. In particular, for the $Ce_{0.5}O_2$:50%Cu^{2+} sample, which can decrease the reaction temperature of CO to 100 °C with the conversion rate reaching 100% (T_{100}), this temperature is much lower than the formerly reported kinds of $Ce_{1-x}O_2$:x%Cu^{2+} composites. Meanwhile, the photocatalytic activity of the synthesized $Ce_{1-x}O_2$:x%Cu^{2+} composites in the degradation of organic dyes was also evaluated, and the results indicate that under the same conditions, the photocatalytic activity of the synthesized $Ce_{1-x}O_2$:x%Cu^{2+} composites was much better than that of other species. In short, all results indicate that the synthesized $Ce_{1-x}O_2$:x%Cu^{2+} nanobelt composite catalysts may have potential applications in the catalyst field.

2. EXPERIMENTAL PROCEDURES

2.1. Materials and Reagents. $Ce(NO_3)_3$·$6H_2O$ (99.9%) was purchased from Aladdin Industrial Inc. $Cu(NO_3)_2$·$3H_2O$ (99.9%) was obtained from Shanghai Jingbao Chemical Corp. Citric acid monohydrate ($C_6H_8O_7$·H_2O) (CA) was provided by Beijing Chemical Corp. All reagents were of analytical grade and used as received without further purification. The filter papers were obtained from Hangzhou Wohua Filter Paper Co.,

Ltd.; before being used as the scaffold, they were washed by suction filtration of ethanol, followed by drying with airflow.

2.2. Synthesis of CeO_2 and CeO_2−CuO Nanobelts. First, 10 mmol of $Ce(NO_3)_3$ and 15 mmol of CA were dissolved in certain volumes (20, 30, and 40 mL) of deionized water to obtain the solution with different concentrations (0.5, 0.33, and 0.25 M), and the obtained solution was maintained at 65 °C for 24 h to form the final sol solution. The preparation of $Ce_{1-x}(NO_3)_3$:x%Cu^{2+} sol solution was similar to that of $Ce(NO_3)_3$ sol solution except for the use of certain amounts (molar) of $Cu(NO_3)_2$ to substitute $Ce(NO_3)_3$.

One typical synthesis procedure of the $Ce_{1-x}O_2$:x%Cu^{2+} nanobelts was as follows: first, a piece of pretreated filter paper was placed in a suction filtering unit. Then, $Ce_{1-x}(NO_3)_3$:x%Cu^{2+} sol solution with different concentrations was passed through the filter paper. The obtained filter paper was washed using ethanol to remove the surface sol solution. Finally, the filter paper was dried in flowing air, and thin $Ce_{1-x}(NO_3)_3$:x%Cu^{2+} gel layers covering the surface of the cellulose fibers were obtained. The resultant $Ce_{1-x}(NO_3)_3$:x%Cu^{2+}/filter paper composites were calcined at 500 °C for 2 h in air to obtain $Ce_{1-x}O_2$:x%Cu^{2+} composites.

2.3. Catalytic Performance on CO. The catalytic performance of $Ce_{1-x}O_2$:x%Cu^{2+} composites on CO was evaluated in a fixed-bed glass reactor using 200 mg of composites and a total inlet flow of 100 mL/min, with 0.5% CO, 10% O_2, and 89.5% Ar. The catalytic performance was evaluated at several temperatures in the range from room temperature to 260 °C. The catalyst was directly exposed to the reaction gas as the reactor temperature was stabilized at the reaction temperature without any pretreatment. The reaction temperature was monitored by a thermocouple placed in the middle of the catalyst bed. The CO concentration in the reactor effluent was analyzed using a Jindao GC-8A gas chromatograph.

2.4. Photocatalytic Performances on Rhodamine B. The photocatalytic activity of the synthesized $Ce_{1-x}O_2$:x%Cu^{2+} composites on rhodamine B (RhB) was conducted in a 250 mL cylindrical glass vessel with a 300 W halogen tungsten lamp as the light source ($\lambda \geq 400$ nm). In a typical photocatalytic experiment, 25 mg of $Ce_{1-x}O_2$:x%Cu^{2+} composites were dispersed in 50 mL of RhB (20 mg/L) and H_2O_2 (5 mL) solution under ultrasonication for 5 min. Then, the mixture was placed in a dark environment with 1 h stirring to obtain adsorption−desorption equilibrium. Every 15 min, 5 mL of suspension was extracted and centrifuged to separate the photocatalyst materials. The UV−vis spectra of the supernatant were recorded using an Agilent Cary 100 to determine the concentration of RhB at each time point.

2.5. Other Characterizations. TG measurements were operated on a Pyris Diamond TG with a heating rate of 10 °C/min from 40 to 800 °C. XRD patterns were measured using a Rigaku-D X-ray powder diffractometer with Cu Kα radiation ($\lambda = 1.54$ Å). The SEM imaging of the products was examined using a field-emission SEM (HITACHI SU8010). Transmission electron microscopy (TEM) and high-resolution TEM (HRTEM) imaging were obtained on a JEOL-2100 microscope with an accelerating voltage of 200 kV. XPS experiments were carried out using an ESCALAB 250 spectrometer. The spectra were recorded using monochromatic Al Kα radiation ($h\nu = 1486.6$ eV) as the excitation source. Photoelectrons were selected in energy with a hemispheric electron analyzer. All of the binding energy (BE) values were referenced to the C 1s
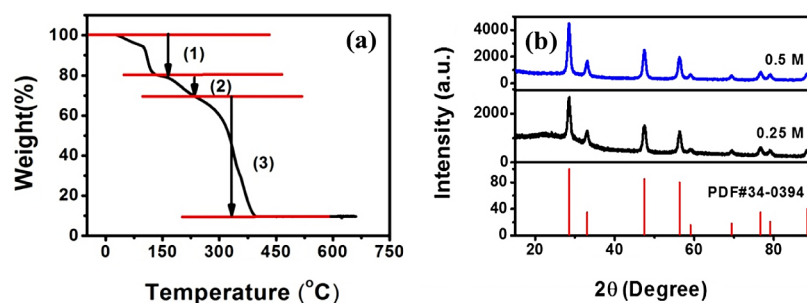
Figure 1. TG curve of the $Ce(NO_3)_3$/filter paper composites (a) and the XRD patterns of the samples prepared using $Ce(NO_3)_3$ sol solution with different concentrations and annealed at 500 °C for 2 h with a temperature increase rate of 1 °C/min (b).

peak of carbon at 284.6 eV. TPR experiments were performed with a thermal conductivity detector, 30 mg samples in a gas mixture of 98% (molar) nitrogen and 2% (molar) hydrogen with a gas flow rate of 100 mL/min, and a temperature range of 80−900 °C with a temperature ramp rate of 5 °C/min. Prior to TPR tests, the samples were treated at 450 °C for 1 h under airflow (ramp rate: 10 °C /min; flow 100 mL/min) to clean the surface.

3. RESULTS AND DISCUSSION

3.1. Phase Structure and Morphology. To find a proper temperature to anneal the $Ce(NO_3)_3$/filter paper composites, TG measurements were first performed. As can be seen in Figure 1a, the result indicates that the weight loss mainly occurs in three stages. The first one below 130 °C corresponds to the release of water molecules adsorbed on the sample, and the weight loss is about 20%. The second one is in the range of 130−200 °C, and the weight loss is about 10%, which may be attributed to the progressive dehydration. The third one ranging from 200 to 500 °C with weight loss about 60% should be ascribed to the burning of filter paper, the decomposition of the organic reagent, $Ce(NO_3)_3$, and the formation of CeO_2. Based on the above TG results, 500 °C was chosen as the annealing temperature because the sample has reached equilibrium before this temperature. Then, an annealing treatment at 500 °C for 2 h with a temperature increase rate of 1 °C/min was performed for the $Ce(NO_3)_3$/filter paper composites. The phase structure as well as the morphology of the obtained samples with different concentrations was characterized. Figure 1b displays the XRD patterns of the annealed samples prepared using $Ce(NO_3)_3$ sol solution with two different concentrations, which shows that the formation of pure CeO_2 with all diffraction peaks is in good agreement with those of the cubic CeO_2 in the JCPDS file PDF no. 34-0394, and no other phase structure can be observed. Meanwhile, it can also be observed that the concentration of $Ce(NO_3)_3$ in sol solution can influence the peak intensity of the obtained XRD patterns. When the $Ce(NO_3)_3$ concentration in the sol solution decreased to half, the peak intensity of the corresponding XRD pattern also decreased nearly half, and this phenomenon should be due to the decrease in the belt's thickness, which further influences the crystal structure. Meanwhile, the crystallite size of the two samples was estimated using Scherrer's equation $D = 0.89\lambda/(\beta \cos\theta)$, in which D is the average grain size, the factor 0.89 is the characteristic of spherical objects, λ is the X-ray wavelength (0.15405 nm), and β and θ are the full width at half-maximum and diffraction angle of the observed peak, respectively. The strongest peak (111) at 2θ (28.555°) was used to calculate the

average crystallite size of the calcined CeO_2 samples, which decreased with decreasing the $Ce(NO_3)_3$ concentration (100 nm for 0.5 M and 71 nm for 0.25 M). This speculation can be further confirmed through the SEM images in Figure 3.
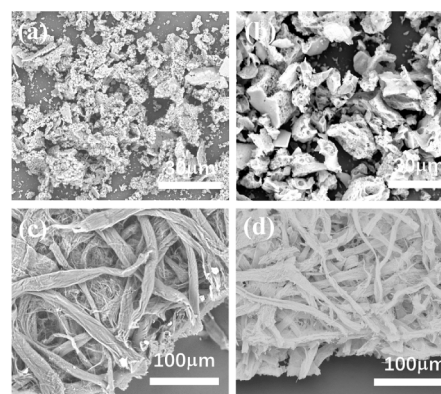

Figure 2. SEM imaging of (a) BM, (b) BMCA, (c) filter paper, and (d) CeO_2 nanobelts.
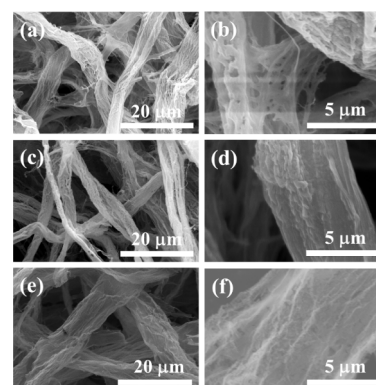
Figure 3. SEM images of the annealed CeO_2 samples prepared using different concentrations of $Ce(NO_3)_3$ sol solution: (a,b) 0.5, (c,d) 0.33, and (e,f) 0.25 M.

The SEM imaging of CeO_2 obtained under different conditions as well as filter paper used in the synthesis was first characterized. The SEM imaging in Figure 2 displays the possible influential factor of CA and filter paper on the morphology of the final sample, while the SEM imaging in Figure S1 depicts the variation process of the synthesized samples. Compared with the CeO_2 prepared without CA and filter paper (BM) (Figure 2a), it can be found that there are a large number of holes in the CeO_2 prepared with CA and
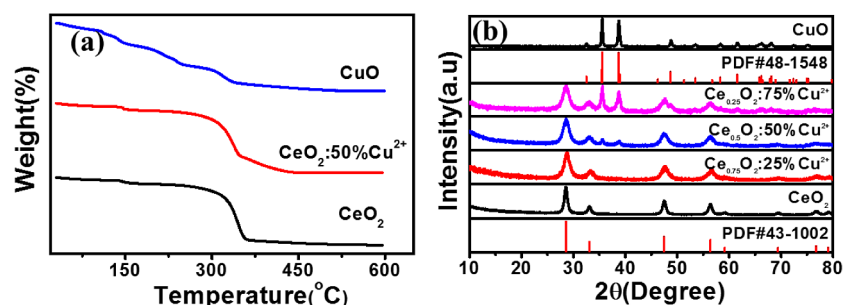
Figure 4. (a) TG curves of the synthesized $Ce_{1-x}(NO_3)_3$:x%Cu^{2+}/filter paper composite with different doping amounts of Cu^{2+} ions. (b) XRD patterns of $Ce_{1-x}O_2$:x%Cu^{2+} composites.

without filter paper as scaffolds (BMCA) besides the increasing size (Figure 2b). This may be due to the existence of CA, which makes the solution more viscous and leaves a large number of holes at high temperature. However, only particles with different sizes can be obtained for the sample of BM and BMCA, and no belt structure can be observed. When filter paper was used as scaffolds, it can be found that the morphology of the obtained CeO_2 is similar with that of the cellulose fiber of the filter paper (Figure 2c,d), indicating that the usage of filter paper can change the final morphology of CeO_2 sample. The morphology changes of the filter paper shown in Figure S1 further confirm the using of filter paper as scaffolds can change the morphology of the final CeO_2 sample.

Then, the influence of $Ce(NO_3)_3$ concentration in the sol solution on the thickness and surface morphology of the final CeO_2 microbelts was studied and is shown in Figure 3. When the $Ce(NO_3)_3$ concentration was controlled at 0.5 or 0.33 M, the annealed samples displayed narrow, uneven microbelts with lots of accumulation and holes on them (Figure 3a–d). When the $Ce(NO_3)_3$ concentration was decreased to 0.25 M, the product mainly consisted of broad micrometer belts with a relatively smooth surface. Comparing with the former two samples (0.5 and 0.3 M $Ce(NO_3)_3$), the thickness of the film and the number of holes on the film decreased greatly; meanwhile, the breadth of the microbelts increased significantly, as shown in Figure 3e,f. This phenomenon should be due to the obvious shrinking of the microbelts during the annealing treatment, and the original morphology of the microbelts could not be retained well because of the decomposition of large amounts of $Ce(NO_3)_3$, resulting in the obvious shrinkage of microbelts.

Because of the structure complement of CuO and CeO_2 and striking improvement of the catalytic activity when Cu^{2+} ions were doped in CeO_2 nanocomposites, different amounts of Cu^{2+} ions were added in the original 0.25 M $Ce(NO_3)_3$ sol solution to substitute Ce^{3+} ions, and $Ce_{1-x}O_2$:x%Cu^{2+}/filter paper composites were prepared. The TG curves of the synthesized $Ce_{1-x}(NO_3)_3$:x%Cu^{2+}/filter paper composites are shown in Figure 4a. It can be found that the doping amounts of Cu^{2+} ions in the original $Ce(NO_3)_3$ sol solution did not change the balance temperature dramatically, and when the annealing temperature reached 500 °C, all of the samples have reached the equilibrium. Thus, 500 °C was further chosen as the annealing temperature in the following annealing treatments of $Ce_{1-x}(NO_3)_3$:x%Cu^{2+}/filter paper composites. Then, the XRD patterns of the annealed samples with different doping amounts of Cu^{2+} ions were characterized. As shown in Figure 4b, it can be observed that when the doping amounts of Cu^{2+} ions are small (25%), the peaks of CuO are too weak to be

observed. With an increase in the doping amounts of Cu^{2+} ions, the peaks ascribed to CuO become obvious gradually. When the doping amounts of Cu^{2+} ions are increased to 50%, the diffraction peaks of CuO can be observed in the XRD pattern besides the peaks of CeO_2, which can be indexed to PDF card no. 43-1548. The intensity of the CuO diffraction peaks increases with an increase in the doping amounts of Cu^{2+} ions. When the doping amounts of Cu^{2+} ions are increased to 100%, pure CuO can be obtained with no other phase structures, indicating that the pure cubic CuO was formed. Furthermore, it can be found that the diffraction peaks become broader for $Ce_{1-x}O_2$:x%Cu^{2+} composites compared with pure CeO_2 or pure CuO films. This should be due to the change in the morphology and size of the synthesized $Ce_{1-x}O_2$:x%Cu^{2+} composites, which can be confirmed by the following SEM, TEM, and HRTEM imaging of the samples (Figures 5 and 6).

The SEM imaging of the synthesized $Ce_{1-x}O_2$:x%Cu^{2+} composites is first executed to verify the possible influence on the morphology by doping Cu^{2+} ions, and the obtained results are shown in Figure 5. Compared with the SEM images of pure CeO_2 (Figure 5a,b), it can be found that the doping of
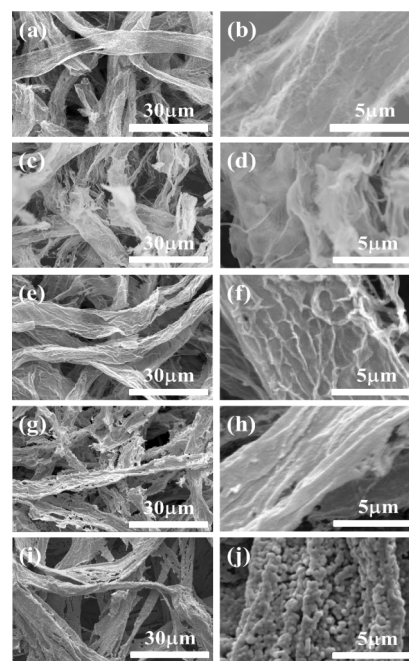
Figure 5. SEM images of the composites: (a,b) CeO_2, (c,d) $Ce_{0.75}O_2$:25%Cu^{2+}, (e,f) $Ce_{0.5}O_2$:50%Cu^{2+}, (g,h) $Ce_{0.25}O_2$:75% Cu^{2+}, and (i,j) CuO.
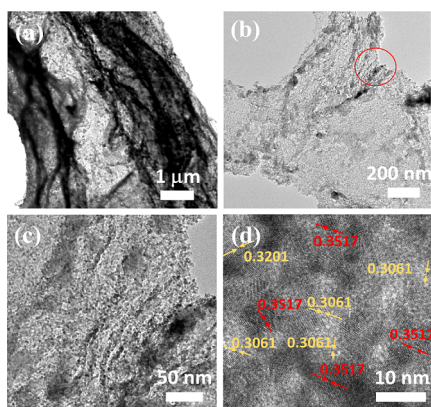
Figure 6. TEM images with different magnifications: (a) 5000×, (b) 20 000×, and (c) 80 000×. (d) HRTEM images of the $Ce_{0.5}O_2$:50% Cu^{2+} nanobelts.

little amounts of Cu^{2+} ions can increase the number of the surface rumples in a certain degree (Figure 5c−f). When the doping amount of Cu^{2+} ions increases to 50% (Figure 5e,f), many rumples can be observed in the images, which can increase the surface areas of the samples and further enhance the catalyst properties of the sample by supplying more active sites. However, the number of the surface rumples can hardly increase always with an increase in the doping amounts of Cu^{2+} ions. When the amounts of Cu^{2+} ions increase to 75% (Figure 5g,h), the integrity of the film is destroyed, and many holes can be observed in the microbelts. In the amplified imaging (Figure 5h), it can be found that surface rumples decrease dramatically and many detritus and particles coexist in the microbelts. For pure CuO (Figure 5i,j), it can be found that the microbelts are composed of CuO microparticles. These changes in the morphology should be due to an increase in Cu^{2+} ions, which separate from the CeO_2 matrix and form tenorite (CuO) particles. The separation of CuO further influences the catalyst

properties of the sample, and this speculation is verified in the following catalyst evaluation.

Meanwhile, the TEM and HRTEM images of $Ce_{0.5}O_2$:50% Cu^{2+} composites are further characterized to study the details. As shown in Figure 6, the TEM imaging (Figure 6a−c) further confirms the repeat of the morphology of the cellulose fibers, and many dark fiber-like parts can be observed (Figure 6a). Besides, from the enlarged part of the TEM image (Figure 6c), it can be found that many nanoparticles with size of about 3−5 nm exist in the film uniformly. HRTEM imaging indicates that two kinds of lattice fringes with different d spacings can be observed; for instance, the lattice fringes with a d spacing of 0.3517 nm belong to the lattice fringe of the [113] plane of CuO, while the lattice fringes with a d spacing of 0.306 nm belong to the lattice fringe of the [311] plane of CeO_2. Combining the TEM image shown in Figure 6c, it can be concluded that the nanoparticles should be CuO, which disperse in CeO_2 nanobelts uniformly.

Then, the possible influence of the doped Cu^{2+} ions on the valence state of the composites was also studied, and XPS of the $Ce_{0.5}O_2$:50%Cu^{2+} composites was performed. Figure 7 depicts the characteristic spin−orbit split of Cu 2p, Ce 3d, O 1s, and C 1s signals for the synthesized composite. As shown, all of the Cu 2p profiles present two sets of peaks, corresponding to Cu $2p_{3/2}$ and Cu $2p_{1/2}$. A broad Cu $2p_{3/2}$ signal composing of two contributions centered at 932.7 (1) and 934.9 eV (2), accompanied by a shakeup satellite in the 939−946 eV region (3 and 4), can be observed. According to previous results,[32] the two peaks centered at 932.7 (1) and 934.9 eV (2) should be ascribed to Cu^{2+} and reduced copper species (Cu^+ or Cu^0). However, the chemical states of Cu^+ and Cu^0, whose peaks appear at 932.4 and 932.6 eV, are not distinguishable on the basis of their Cu $2p_{3/2}$ BE.[33] The Auger Cu LMM was further measured to distinguish the different species of Cu (Figure 7; Cu LMM). It can be found that two peaks can be observed in the spectrum: a weak peak at 916 eV
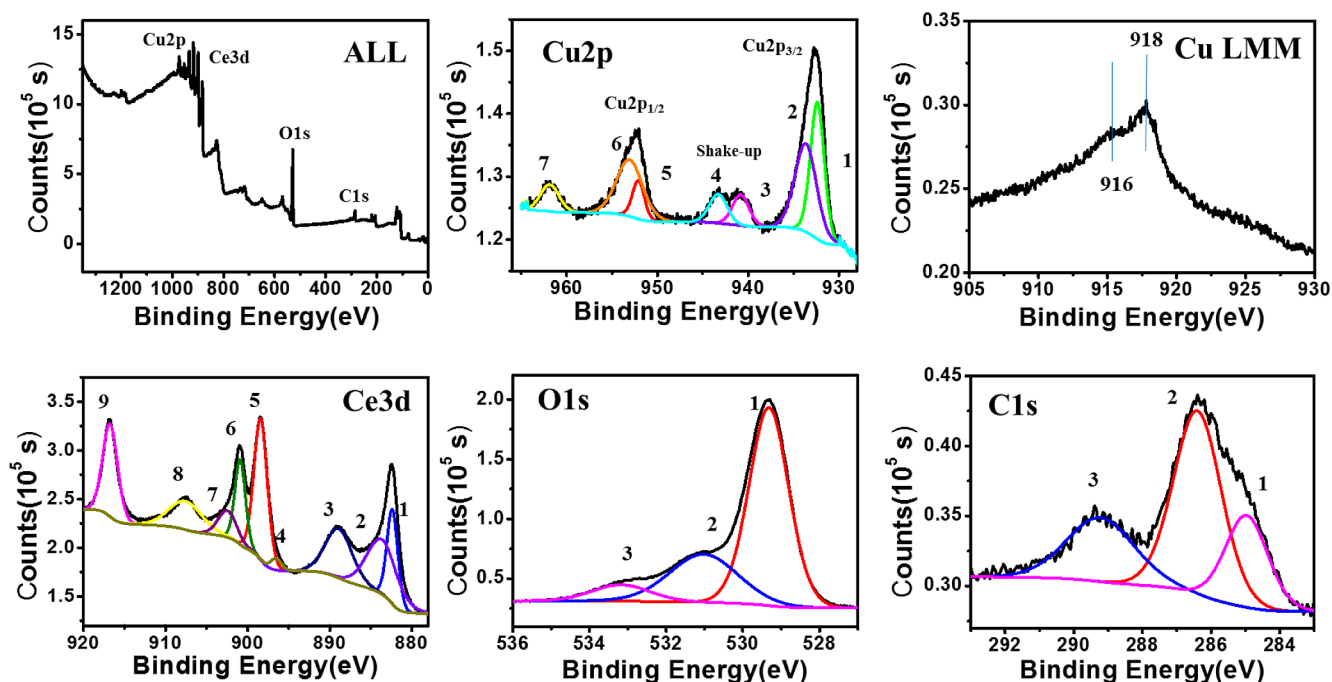
Figure 7. XPS of the synthesized $Ce_{0.5}O_2$:50%Cu^{2+} nanobelts and Cu LMM.
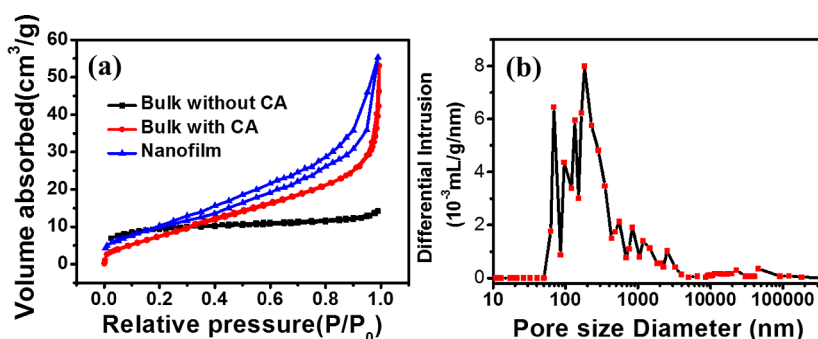
Figure 8. (a) N_2 adsorption−desorption isotherms of the synthesized $Ce_{0.5}O_2$:50%Cu^{2+} nanobelts: $Ce_{0.5}O_2$:50%Cu^{2+} BMCA and $Ce_{0.5}O_2$:50%Cu^{2+} BM. (b) Pore size distribution curve of the synthesized $Ce_{0.5}O_2$:50%Cu^{2+} nanobelts.
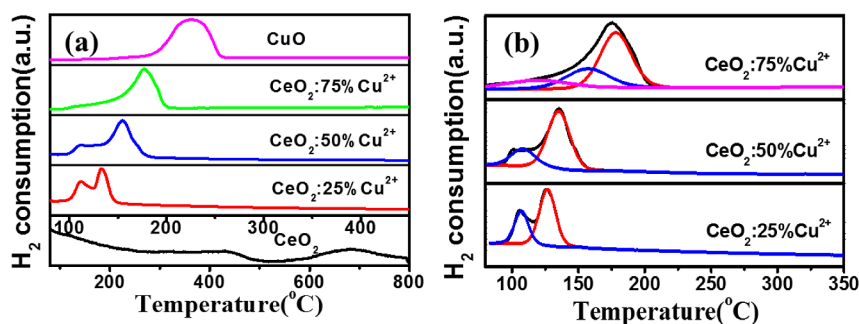
Figure 9. (a) TPR curves of $Ce_{1−x}O_2$:x%Cu^{2+} composites as well as the peak fit of the TPR curves of CeO_2:25%Cu^{2+}, CeO_2:50%Cu^{2+}, and CeO_2:75%Cu^{2+} (b).

should correspond to Cu^+, while the other one at ~918 eV should be ascribed to Cu^{2+}. It is reasonable to speculate that the presence of reduced states (Cu^+ or Cu^0) should depend on the preparation method, especially the existence of citric acid, which has reduction ability. Meanwhile, the formation of Cu^+ might also be induced by substitution at the interface of the two oxide phases because of the analogous Ce^{4+} and Cu^+ ionic radii.[34] The Ce 3d spectrum is known to be complicated because of the hybridization of the Ce 4f with ligand O 2p orbitals and fractional occupancy of the valence 4f orbitals. The spectra can be decomposed in nine contributions: 1 and 6 (Ce $3d^94f^2$, O $2p^4$) and 3 and 8 (Ce $3d^94f^1$, O $2p^5$); 5 and 9 (final state of Ce $3d^94f^0$, O $2p^6$) assigned to Ce(IV); 4 (Ce $3d^94f^2$, O $2p^5$) and 2 and 7(Ce $3d^94f^1$, O $2p^6$) assigned to Ce(III). The peaks 1, 3, 5, 6, 7, and 9 are associated with the Ce^{4+} initial state, while the peaks 2, 4, and 7 are ascribed to the Ce^{3+} initial state of CeO_2. It is believed that the reducibility of Ce^{4+} to Ce^{3+} forces the copper ions to adapt to a different oxidation state, maintaining the charge balance of the lattice. Therefore, it is reasonable to suggest that the redox cycles between Ce^{4+}/Ce^{3+} and Cu^{2+}/Cu^+ are more facile to occur in this process and play an important role in the catalytic reaction.[35] The O 1s XPS data exhibit a main peak (1) at 529 eV and two smaller peaks (2 and 3) located at 531 and 533 eV, respectively. The main peak (1) can be ascribed to the lattice oxygen of CeO_2 and CuO, and the shoulder peak (2) can be attributed to surface chemisorbed oxygen, which contains $O^−$, $O^{2−}$, $O_2^{2−}$, etc. Meanwhile, the smaller peak (3) can be attributed to covalent oxygen, such as surface H_2O and CO_2.[36] The C 1s spectra have similar features to those of O 1s spectra, which contain a main peak (1) at 284.5 eV and two smaller peaks (2 and 3) at 286 and 288.8 eV, respectively. The main peak (1) can be ascribed to C−C, and the shoulder peak (2) can be attributed to C−O, while the smaller peak (3) can be

attributed to O=C−C. The existence of C should be due to the addition of citric acid in the raw materials as well as the CO_2 in the air. The energy-dispersive X-ray spectra of the as-synthesized $Ce_{0.5}O_2$:50%Cu^{2+} nanobelts and the corresponding $Ce_{0.5}O_2$:50%Cu^{2+} BMCA further confirm the presence of element C in the sample (Figure S2c,d).

For being a potential catalyst, it is well known that the specific surface area is an important parameter that can influence the number of active sites. The N_2 adsorption−desorption isotherms of the synthesized $Ce_{0.5}O_2$:50%Cu^{2+} nanobelts as well as the corresponding bulk material are synthesized with CA (BMCA) and without CA (BM). As shown in Figure 8a, the Brunauer−Emmett−Teller (BET) surface area of the nanobelts is measured to be 58 m^2/g (BJH desorption), which is much higher than 31 m^2/g of BMCA and 23 m^2/g of the BM, combining the SEM imaging of the three samples; the addition of CA and the usage of the filter paper as scaffolds facilitate the improvement of the BET surface area. Besides, the pore size distribution curve of the synthesized $Ce_{0.5}O_2$:50%Cu^{2+} nanobelts was also measured through mercury intrusion porosimetry (Figure 8b), and the results indicate that the obtained nanobelts have large macroporosity, mainly in the range of 50−400 nm. All of these results indicate that the special nanobelt structure of $Ce_{1−x}O_2$:x%Cu^{2+} composites can supply much more active sites. Then, the evaluation of the catalytic properties of the obtained $Ce_{1−x}O_2$:x%Cu^{2+} composites was executed, including their catalytic properties for CO oxidation and photocatalytic activity for RhB.

3.2. Catalytic Performance on CO. The H_2−TPR profiles of the nanobelts with different doping amounts of Cu^{2+} ions are compared in Figure 9. For the pure CeO_2 sample, two weak peaks can be observed in the high-temperature area centered at 427 and 688 °C. The low-

temperature peak accounts for the surface reduction of cerium atoms from the +4 to +3 oxidation state,[37,38] while the peak at a higher temperature corresponds to the reduction of ceria bulk. They are associated with the reduction of surface capping oxygen and bulk oxygen atoms, respectively. Besides, the position of the reduction peak is much lower than those reported at 450 and 900 °C.[39] For the synthesized CuO sample, a single peak can be observed at around 220 °C, which is also much lower than that reported at 380 °C.[27] Compared with the CeO_2 and CuO profiles, the profiles of $Ce_{1-x}O_2$:x%Cu^{2+} nanobelts show a strong reduction peak in the lower temperature region (Figure 9a,b). Two or three overlapped reduction peaks in the low-temperature reduction region indicate that different copper species are present in the samples. As reported,[40] the peaks located below ∼160 °C should be associated with the presence of the most easily reducible CuO species, which is highly dispersed on the surface of the nanobelts or interacting strongly with ceria, whereas the peaks located in the range of 160−200 °C should be due to larger CuO particles. Finally, the peak centered around ∼220 °C should be assigned to the reduction of bulk CuO. It can be found that when the doping amounts of Cu^{2+} are lower than 50%, the peaks are mainly located lower than 160 °C, indicating the excellent dispersion of CuO on the nanobelts and good interaction with ceria. When the doping amounts of Cu^{2+} reach 75%, the position of the peaks red-shift to high temperatures, around 200 °C, indicating the increase in the size of CuO particles. However, this temperature is still much lower than that of literature, which reported the position of the reduction peak was in the ranged of 150−280 °C,[19] combining with the reduction peak positions of pure CeO_2 and CuO, which are also much lower than that reported previously,[27,39] it can be concluded that the special nanobelt structure can make the reduction peak shift to low temperatures. These results display that the presence of Cu^{2+} ions can affect both the surface redox properties of CeO_2 and the bulk ones, as demonstrated by Martinez-Arias et al.[36,39] The redox properties of Cu^{2+} and Ce^{4+} are mutually affected by the presence of each other, and which further influence their sequential catalyst properties.

Then, the catalytic activities of $Ce_{1-x}O_2$:x%Cu^{2+} nanobelts on CO as a function of reaction temperature were determined, and the obtained results are shown in Figure 10. It can be noted that the CO conversion rate increases with an increase in the reaction temperature for all samples. For the full CO conversion rate 100% (T_{100}), the temperatures needed for different samples are also different. It is only at 100 °C can the CeO_2:50%Cu^{2+} sample make the CO conversion rate reach
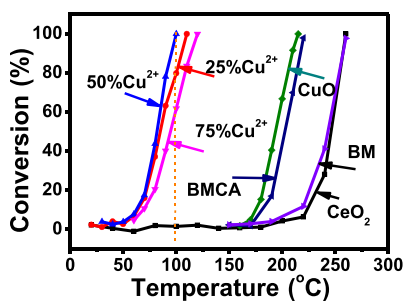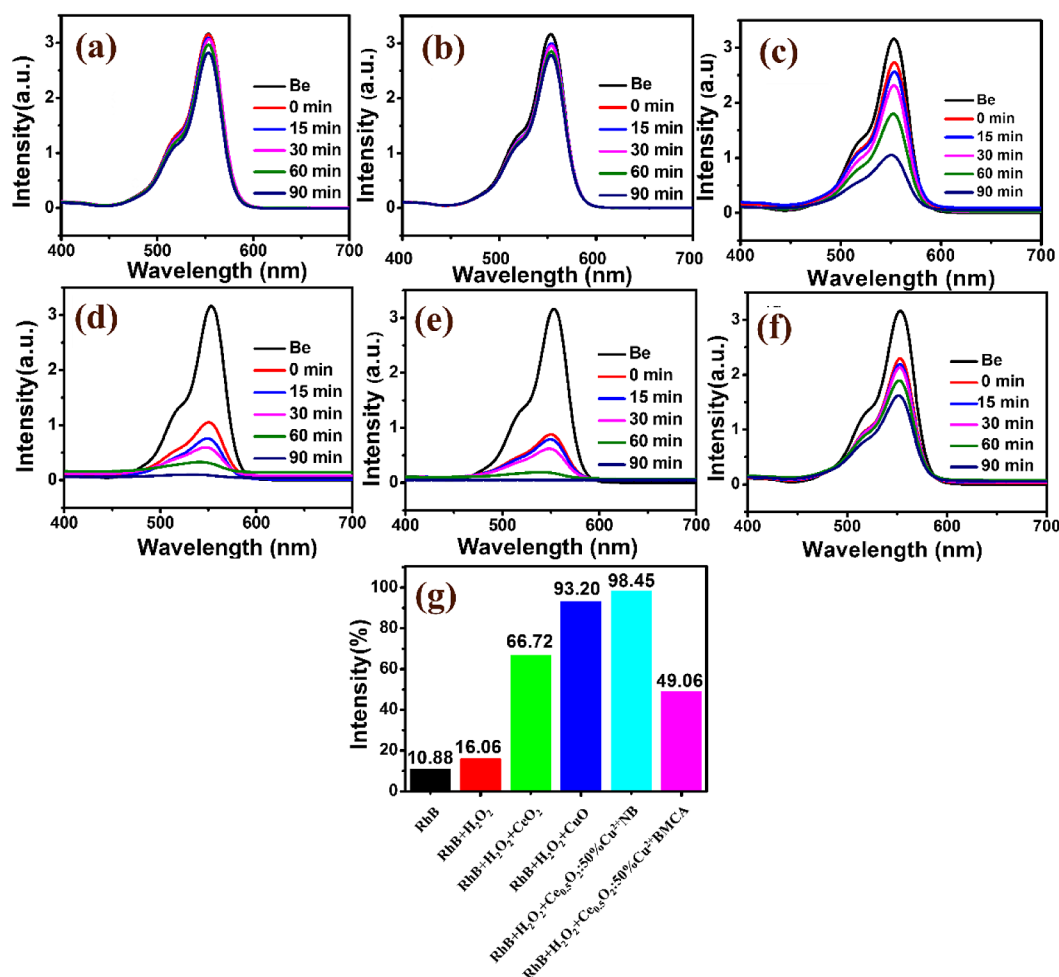
100%. This temperature is much lower than those of other samples. For the selected five $Ce_{1-x}O_2$:x%Cu^{2+} nanobelts and two corresponding bulk materials (BMCA and BM), the needed temperatures to make the conversion rate of CO reach 100% are as follows: $Ce_{0.5}O_2$:50%Cu^{2+} (100 °C) < $Ce_{0.75}O_2$:25%Cu^{2+} (109 °C) < $Ce_{0.25}O_2$:75%Cu^{2+} (121 °C) < CuO (221 °C) < $Ce_{0.5}O_2$:50%Cu^{2+} BMCA (223 °C) < CeO_2 (261 °C) < $Ce_{0.5}O_2$:50%Cu^{2+} BM (261 °C, 98%). These results indicate that the complex nanobelts of CeO_2 and CuO can improve their catalytic activities on CO conversion than those of pure CeO_2 or CuO nanobelts as well as the corresponding bulk materials with different morphologies. Meanwhile, the synthesized $Ce_{1-x}O_2$:x%Cu^{2+} nanobelts also show better catalytic activity and lower temperature than the previously reported catalysts used for CO conversion, such as CeO_2:Au catalyst, (165 °C),[39] CuO-doped CeO_2 nano-particles (140 °C),[19] copper−ceria nanosheets (122 °C),[41] Cu−ceria nanorods (125 °C),[42] and so on, with the CO conversion rate reaching 100%. The better catalytic property in our samples should be due to the better synergistic interaction between CuO and CeO_2 in this nanobelt structure, which is responsible for the higher activity.

3.3. Photochemical Performances on Rhodamine B. CuO nanomaterials are also well known for their photo-catalytic activity, which can be used in the photodegradation of organic dyes under the irradiation of visible light at an ambient temperature.[43] In this paper, the photocatalytic activity of $Ce_{1-x}O_2$:x%Cu^{2+} complex nanobelts was also evaluated. RhB was chosen as a degradation sample under the irradiation of visible light at an ambient temperature in the presence of hydroxide water (H_2O_2). The characteristic absorption peak of RhB at 553 nm is monitored to follow the catalytic degradation process, and the optical absorption spectra of RhB measured at different intervals are shown in Figure 11. For pure RhB aqueous solution, only a slight degradation of RhB (10.88%) can be detected after 90 min irradiation (Figure 11a). Figure 11b shows the optical absorption spectra of RhB measured at different intervals only with the H_2O_2; only 16.06% RhB can be degraded after 90 min irradiation (Figure 11b). The addition of CeO_2 to the RhB and H_2O_2 solution can enhance the degradation level of RhB, and about 66.72% RhB can be degraded after 90 min irradiation (Figure 11c). The degradation degree of RhB by adding pure CuO to the solution of RhB and H_2O_2 is higher than that of CeO_2, and about 93.2% RhB can be degraded after 90 min irradiation (Figure 11d). The degradation performance of the CeO_2:50% Cu^{2+} complex nanobelts is better than that of pure CuO, and about 98.43% RhB can be degraded after 90 min irradiation (Figure 11e). Meanwhile, the photodegradation property of CeO_2:50%Cu^{2+} BMCA was also evaluated, and only about 49.06% RhB can be degraded after 90 min irradiation, which is much lower than that of the CeO_2:50%Cu^{2+} complex nanobelts. Thus, the degradation degree of RhB at 90 min in the presence of the above four $Ce_{1-x}O_2$:x%Cu^{2+} samples is as follows: $Ce_{0.5}O_2$:50%Cu^{2+} nanobelts (98.43%) > CuO film (93.2%) > CeO_2 film (66.72%) > $Ce_{0.5}O_2$:50%Cu^{2+} BMCA (49.06%). These results indicate that the complex nanobelts of the CeO_2 and CuO can improve their photochemical performances under the same condition (Figure 11c−e). Meanwhile, the morphology of the samples also plays an important role in the catalytic performance (Figure 11e,f), and the nanobelt structure of the sample has better photocatalytic activity. This should be due to the higher BET surface area of

Figure 10. Catalytic activities of $Ce_{1-x}O_2$:x%Cu^{2+} nanobelts, $Ce_{0.5}O_2$:50%Cu^{2+} BMCA, and $Ce_{0.5}O_2$:50%Cu^{2+} BM on CO as a function of reaction temperature.

Figure 11. Absorption spectra of RhB under the irradiation of visible light with different catalyst samples. (a) Without any catalyst and H_2O_2, (b) H_2O_2, (c) CeO_2 and H_2O_2, (d) CuO and H_2O_2, (e) $Ce_{0.5}O_2$:50%Cu^{2+} nanobelts and H_2O_2, and (f) $Ce_{0.5}O_2$:50%Cu^{2+} BMCA and H_2O_2. (g) Plot of the extent of photodegradation of RhB, which corresponds to (a−f).
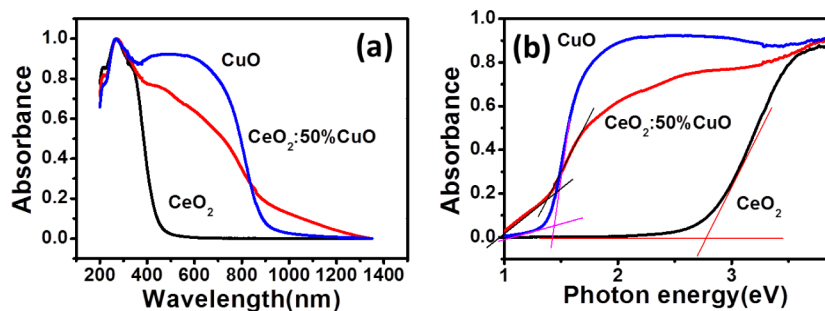
Figure 12. (a) UV−vis spectra and (b) plot of photon energy of the as-prepared CeO_2, $Ce_{0.5}O_2$:50%Cu^{2+}, and CuO products.

nanobelts structure of the sample, which can supply more catalytic sites.

To verify these results, the optical energy band gaps of the synthesized CeO_2, $Ce_{0.5}O_2$:50%Cu^{2+}, and CuO nanobelts were further studied, and their UV−vis spectra were characterized. As shown in Figure 12a,b, it can be found that the UV−visible spectra of the as-prepared CeO_2 products occur at 460 nm, while the UV−visible spectra of the as-prepared CuO products occur at 910 nm, which is near to that of $Ce_{0.5}O_2$:50%Cu^{2+}. The band gaps of CeO_2, CuO, and $Ce_{0.5}O_2$:50%Cu^{2+} nanobelts are estimated to be 2.75, 1.36, and 1.32 eV, respectively. The

doping of CuO on CeO_2 nanobelts can decrease its band gap, which can further enhance the photochemical performances.

The fundamental photodegradation mechanism involves the acceleration in the decomposition of H_2O_2 over the catalyst to generate free-radical species, such as $^\bullet OH$, $^\bullet OOH$, or $^\bullet O^{2-}$, which are deemed to be liable for the degradation of the dyes. The related chemical reactions including the electrons (e^-) in the VB can be excited to the CB and at the same time can generate the same number of holes (h^+) in the VB. The formed e^- and h^+ pairs can be captured by H_2O_2 molecules, leading to the formation of $^\bullet OH$, $^\bullet HOO$, or $^\bullet O^{2-}$; oxidant species react

with dye and finally realize complete mineralization with the formation of CO_2, H_2O, or other inorganic ions.[19]

To investigate the possible mechanism for the enhancement of the catalytic performance of the $Ce_{1−x}O_2$:x%Cu^{2+} complex film, the crystal structure of CeO_2 and CuO are studied, and their simulated crystal structures are displayed in Figure 13. It
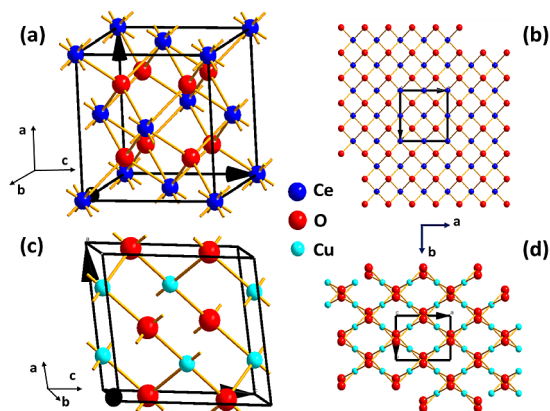
Figure 13. Simulated crystal structures of CeO_2 and CuO. (a) Crystal structure of CeO_2. (b) Packing view along the c axis of CeO_2. (c) Crystal structure of CuO. (d) Packing view along the c axis of CuO.

is known that CeO_2 is of a cubic fluorite structure (space group $Fm3m$) with a lattice constant of $a = 0.541$ nm (Figure 13a,b). Ce^{4+} ions arranged with a face-centered cubic phase and $O^{2−}$ atoms occupy all tetrahedra in the cell. Each Ce atom is surrounded by eight O atoms, and every O atom can form ligand bonds with four Ce atoms. This structure is also called as an open structure as there are many cubic spaces in it, and ions can disperse quickly in this crystal structure. For monoclinic CuO (Figure 13c,d), the crystal can be described as alternating planes composed of $O^{2−}$ and Cu^{2+} ions, which are stacked alternately along the [002] axis. The oppositely charged ions form positively charged (002)-Cu and negatively charged (002)-O polar on the two sides. For the $Ce_{1−x}O_2$:x%Cu^{2+} complex nanobelts, the O atoms in CeO_2 cell can be easily lost, and the presence of oxygen vacancies in the remaining $CeO_{2−x}$ cell can induce the charge variation of a small amount of the copper in the lattice as a consequence of charge compensation upon the incorporation of Cu^{2+}. Alternatively, the remaining $CeO_{2−x}$ can also be easily oxidized into CeO_2 and further reduce the charge variation of the surrounding ions.[44,45] Thus, the active sites at the interface between CuO and CeO_2 cyclic changed. For the improvement of the catalytic performance of the synthesized $Ce_{0.5}O_2$:50%Cu^{2+} nanobelts than the other species, especially the bulk materials, there are mainly several reasons. First, the increasing of the amount of interfacial active sites of $Ce_{0.5}O_2$:50%Cu^{2+} film by increasing the surface area and the doping amounts of Cu^{2+}. Second, the changing of the physicochemical properties of the $Ce_{0.5}O_2$:50%Cu^{2+} on the exposed face, which can also influence the catalytic performance of the final sample.

4. CONCLUSIONS

In this paper, a new method was attempted for the synthesis of CeO_2 films using commercial filter papers as the scaffold, and Cu^{2+} ions were doped in the original $Ce(NO_3)_3$ sol solution to prepare $Ce_{1−x}O_2$:x%Cu^{2+} complex nanobelt catalysts. The SEM images indicate that there are no separated CuO particles

appearing in the obtained films when the doping amounts of Cu^{2+} ions are no higher than 50% (mol). The H_2−TPR curves and the catalytic evaluation results display that the obtained $Ce_{1−x}O_2$:x%Cu^{2+} catalysts have excellent catalyst property for CO oxidation. Especially for the $Ce_{0.5}O_2$:50%Cu^{2+} sample, which can decrease the reaction temperature of CO to 100 °C with the conversion rate reaching to 100%, this temperature was much lower than the formerly reported $Ce_{1−x}O_2$:x%Cu^{2+} catalysts or other metal ion-doped CeO_2 matrix. Meanwhile, the synthesized $Ce_{0.5}O_2$:50%Cu^{2+} has also enhanced photochemical performance compared with pure CeO_2 or CuO belts obtained under the same condition, and the morphology of the sample can also influence the catalytic properties. These results indicate that the synthesized $Ce_{1−x}O_2$:x%Cu^{2+} films may find potential applications in the catalyst field. Meanwhile, the demonstrated method also can be extendable to the synthesis of other inorganic oxide compounds.

■ ASSOCIATED CONTENT

Ⓢ Supporting Information

The Supporting Information is available free of charge at https://pubs.acs.org/doi/10.1021/acsomega.1c00487.

> Experimental details, additional figures, and other characterizations (PDF)

■ AUTHOR INFORMATION

Corresponding Authors

Lei Qi − *Institute of Advanced Materials for Nano-bio Applications, School of Ophthalmology and Optometry, Wenzhou Medical University, Wenzhou, Zhejiang Province 325027, China;* Email: imdoll@163.com

Mei Yang − *Institute of Advanced Materials for Nano-bio Applications, School of Ophthalmology and Optometry, Wenzhou Medical University, Wenzhou, Zhejiang Province 325027, China;* Email: meiyang112686@wzmc.edu.cn

Authors

Yida Huang − *Institute of Advanced Materials for Nano-bio Applications, School of Ophthalmology and Optometry, Wenzhou Medical University, Wenzhou, Zhejiang Province 325027, China;* ⓞ orcid.org/0000-0002-3166-0701

Youlong Liang − *Institute of Advanced Materials for Nano-bio Applications, School of Ophthalmology and Optometry, Wenzhou Medical University, Wenzhou, Zhejiang Province 325027, China*

Chaoran Xie − *Institute of Advanced Materials for Nano-bio Applications, School of Ophthalmology and Optometry, Wenzhou Medical University, Wenzhou, Zhejiang Province 325027, China*

Qingyuan Gui − *Institute of Advanced Materials for Nano-bio Applications, School of Ophthalmology and Optometry, Wenzhou Medical University, Wenzhou, Zhejiang Province 325027, China*

Jinlei Ma − *Institute of Advanced Materials for Nano-bio Applications, School of Ophthalmology and Optometry, Wenzhou Medical University, Wenzhou, Zhejiang Province 325027, China*

Hongxian Pan − *Institute of Advanced Materials for Nano-bio Applications, School of Ophthalmology and Optometry, Wenzhou Medical University, Wenzhou, Zhejiang Province 325027, China*

Zeyu Tian − *Institute of Advanced Materials for Nano-bio Applications, School of Ophthalmology and Optometry, Wenzhou Medical University, Wenzhou, Zhejiang Province 325027, China*

Complete contact information is available at:
https://pubs.acs.org/10.1021/acsomega.1c00487

Author Contributions

#Y.H., Y.L., and C.X. contributed equally to this work.

Notes

The authors declare no competing financial interest.

■ REFERENCES

(1) Si, R.; Zhang, Y.-W.; You, L.-P.; Yan, C.-H. Rare-earth oxide nanopolyhedra, nanoplates, and nanodisks. *Angew. Chem., Int. Ed.* **2005**, *44*, 3256−3260.

(2) Wang, Z.; Quan, Z.; Lin, J. Remarkable changes in the optical properties of CeO_2 nanocrystals induced by lanthanide ions doping. *Inorg. Chem.* **2007**, *46*, 5237−5242.

(3) Xia, B.; Lenggoro, I. W.; Okuyama, K. Synthesis of CeO_2 nanoparticles by salt-assisted ultrasonic aerosol decomposition. *J. Mater. Chem.* **2001**, *11*, 2925−2927.

(4) Kaspar, J.; Fornasiero, P.; Graziani, M. Use of CeO_2-based oxides in the three-way catalysis. *Catal. Today* **1999**, *50*, 285−298.

(5) Acuna, L. M.; Munoz, F. F.; Albornoz, C. A.; Leyva, A. G.; Baker, R. T.; Fuentes, R. O. Nanostructured terbium-doped ceria spheres: Effect of dopants on their physical and chemical properties under reducing and oxidizing conditions. *J. Mater. Chem. A* **2015**, *3*, 16120−16131.

(6) Ke, J.; Xiao, J.-W.; Zhu, W.; Liu, H.; Si, R.; Zhang, Y.-W.; Yan, C.-H. Dopant-Induced Modification of Active Site Structure and Surface Bonding Mode for High-Performance Nanocatalysts: CO Oxidation on Capping-free (110)-oriented CeO_2: Ln(Ln = La-Lu) Nanowires. *J. Am. Chem. Soc.* **2013**, *135*, 15191−15200.

(7) Kehoe, A. B.; Scanlon, D. O.; Watson, G. W. Role of Lattice Distortions in the Oxygen Storage Capacity of Divalently Doped CeO_2. *Chem. Mater.* **2011**, *23*, 4464−4468.

(8) Munoz, F. F.; Acuna, L. M.; Albornoz, C. A.; Leyva, A. G.; Baker, R. T.; Fuentes, R. O. Redox properties of nanostructured lanthanide-doped ceria spheres prepared by microwave assisted hydrothermal homogeneous co-precipitation. *Nanoscale* **2015**, *7*, 271−281.

(9) Reddy, B. M.; Katta, L.; Thrimurthulu, G. Novel Nanocrystalline $Ce_{1-x}La_xO_2$-delta (x=0.2) Solid Solutions: Structural Characteristics and Catalytic Performance. *Chem. Mater.* **2010**, *22*, 467−475.

(10) Shan, W.; Dong, X.; Ma, N.; Yao, S.; Feng, Z. The Synthesis of Three-Dimensional CeO_2 and Their Catalytic Activities for CO Oxidation. *Catal. Lett.* **2009**, *131*, 350−355.

(11) Wang, Z.; Li, R.; Chen, Q. Enhanced Activity of CuCeO Catalysts for CO Oxidation: Influence of Cu_2O and the Dispersion of Cu_2O, CuO, and CeO_2. *ChemPhysChem* **2015**, *16*, 2415−2423.

(12) Yang, D.; Wang, L.; Sun, Y.; Zhou, K. Synthesis of One-Dimensional $Ce_{1-x}Y_xO_{2-x/2}$ ($0 \leq x \leq 1$) Solid Solutions and Their Catalytic Properties: The Role of Oxygen Vacancies. *J. Phys. Chem. C* **2010**, *114*, 8926−8932.

(13) Yang, F.; Wei, J.; Liu, W.; Guo, J.; Yang, Y. Copper doped ceria nanospheres: Surface defects promoted catalytic activity and a versatile approach. *J. Mater. Chem. A* **2014**, *2*, 5662−5667.

(14) Kydd, R.; Teoh, W. Y.; Wong, K.; Wang, Y.; Scott, J.; Zeng, Q.-H.; Yu, A.-B.; Zou, J.; Amal, R. Flame-Synthesized Ceria-Supported Copper Dimers for Preferential Oxidation of CO. *Adv. Funct. Mater.* **2009**, *19*, 369−377.

(15) Tanaka, H.; Kaino, R.; Okumura, K.; Kizuka, T.; Tomishige, K. Catalytic performance and characterization of Rh-CeO_2/MgO catalysts for the catalytic partial oxidation of methane at short contact time. *J. Catal.* **2009**, *268*, 1−8.

(16) Wang, X. Q.; Rodriguez, J. A.; Hanson, J. C.; Gamarra, D.; Martinez-Arias, A.; Fernandez-Garcia, M. In situ studies of the active sites for the water gas shift reaction over Cu-CeO_2 catalysts: Complex interaction between metallic copper and oxygen vacancies of ceria. *J. Phys. Chem. B* **2006**, *110*, 428−434.

(17) Reddy, B. M.; Rao, K. N. Copper promoted ceria-zirconia based bimetallic catalysts for low temperature soot oxidation. *Catal. Commun.* **2009**, *10*, 1350−1353.

(18) Hornes, A.; Hungria, A. B.; Bera, P.; Lopez Camara, A.; Fernandez-Garcia, M.; Martinez-Arias, A.; Barrio, L.; Estrella, M.; Zhou, G.; Fonseca, J. J.; Hanson, J. C.; Rodriguez, J. A. Inverse CeO_2/CuO Catalyst As an Alternative to Classical Direct Configurations for Preferential Oxidation of CO in Hydrogen-Rich Stream. *J. Am. Chem. Soc.* **2010**, *132*, 34−35.

(19) Luo, M.-F.; Ma, J.-M.; Lu, J.-Q.; Song, Y.-P.; Wang, Y.-J. High-surface area CuO-CeO_2 catalysts prepared by a surfactant-templated method for low-temperature CO oxidation. *J. Catal.* **2007**, *246*, 52−59.

(20) Wang, S.; Mao, D.; Guo, X.; Wu, G.; Lu, G. Dimethyl ether synthesis via CO_2 hydrogenation over CuO-TiO_2-ZrO_2/HZSM-5 bifunctional catalysts. *Catal. Commun.* **2009**, *10*, 1367−1370.

(21) Luo, M.-F.; Song, Y.-P.; Lu, J.-Q.; Wang, X.-Y.; Pu, Z.-Y. Identification of CuO species in high surface area CuO-CeO_2 catalysts and their catalytic activities for CO oxidation. *J. Phys. Chem. C* **2007**, *111*, 12686−12692.

(22) Zhang, D.; Qian, Y.; Shi, L.; Mai, H.; Gao, R.; Zhang, J.; Yu, W.; Cao, W. Cu-doped CeO_2 spheres: Synthesis, characterization, and catalytic activity. *Catal. Commun.* **2012**, *26*, 164−168.

(23) Yang, W.; Li, D.; Xu, D.; Wang, X. Effect of CeO_2 preparation method and Cu loading on CuO/CeO_2 catalysts for methane combustion. *J. Nat. Gas Chem.* **2009**, *18*, 458−466.

(24) Ranjith, K. S.; Dong, C.-L.; Lu, Y.-R.; Huang, Y.-C.; Chen, C.-L.; Saravanan, P.; Asokan, K.; Kumar, R. T. R. Evolution of Visible Photocatalytic Properties of Cu-Doped CeO_2 Nanoparticles: Role of Cu^{2+}-Mediated Oxygen Vacancies and the Mixed-Valence States of Ce Ions. *ACS Sustainable Chem. Eng.* **2018**, *6*, 8536−8546.

(25) Luo, M.; Zhong, Y. J.; Yuan, X. X.; Zheng, X. M. TPR and TPD studies of CuOCeO$_2$ catalysts for low temperature CO oxidation. *Appl. Catal., A* **1997**, *162*, 121−131.

(26) Kang, X.; Liu, H.; Hou, M.; Sun, X.; Han, H.; Jiang, T.; Zhang, Z.; Han, B. Synthesis of Supported Ultrafine Non-noble Subnanometer-Scale Metal Particles Derived from Metal-Organic Frameworks as Highly Efficient Heterogeneous Catalysts. *Angew. Chem., Int. Ed.* **2016**, *55*, 1080−1084.

(27) Liu, P.; Zhao, Y.; Qin, R.; Mo, S.; Chen, G.; Gu, L.; Chevrier, D. M.; Zhang, P.; Guo, Q.; Zang, D.; Wu, B.; Fu, G.; Zheng, N. Photochemical route for synthesizing atomically dispersed palladium catalysts. *Science* **2016**, *352*, 797−801.

(28) Shin, Y. S.; Li, X. H. S.; Wang, C. M.; Coleman, J. R.; Exarhos, G. J. Synthesis of hierarchical titanium carbide from titania-coated cellulose paper. *Adv. Mater.* **2004**, *16*, 1212−1215.

(29) Liu, X.; Zhang, Y.; Wu, T.; Huang, J. Hierarchical nanotubular titanium nitride derived from natural cellulose substance and its electrochemical properties. *Chem. Commun.* **2012**, *48*, 9992−9994.

(30) Rao, K. N.; Venkataswamy, P.; Reddy, B. M. Structural Characterization and Catalytic Evaluation of Supported Copper-Ceria Catalysts for Soot Oxidation. *Ind. Eng. Chem. Res.* **2011**, *50*, 11960−11969.

(31) Bera, P.; Priolkar, K. R.; Sarode, P. R.; Hegde, M. S.; Emura, S.; Kumashiro, R.; Lalla, N. P. Structural investigation of combustion synthesized Cu/CeO_2 catalysts by EXAFS and other physical techniques: Formation of a $Ce_{1-x}Cu_xO_2$-delta solid solution. *Chem. Mater.* **2002**, *14*, 3591−3601.

(32) Hocevar, S.; Krasovec, U. O.; Orel, B.; Arico, A. S.; Kim, H. CWO of phenol on two differently prepared $CuO-CeO_2$ catalysts. *Appl. Catal., B* **2000**, *28*, 113−125.

(33) Park, P. W.; Ledford, J. S. Effect of Crystallinity on the Photoreduction of Cerium Oxide: A Study of CeO_2 and Ce/Al_2O_3 Catalysts. *Langmuir* **1996**, *12*, 1794−1799.

(34) Yao, W.-T.; Yu, S.-H.; Zhou, Y.; Jiang, J.; Wu, Q.-S.; Zhang, L.; Jiang, J. Formation of uniform CuO nanorods by spontaneous aggregation: Selective synthesis of CuO, Cu_2O, and Cu nanoparticles by a solid-liquid phase arc discharge process. *J. Phys. Chem. B* **2005**, *109*, 14011−14016.

(35) Tang, X.-L.; Zhang, B.-C.; Li, Y.; Xu, Y.-D.; Xin, Q.; Shen, W.-J. Carbon monoxide oxidation over CuO/CeO_2 catalysts. *Catal. Today* **2004**, *93-95*, 191−198.

(36) Martinez-Arias, A.; Hungria, A. B.; Fernandez-Garcia, M.; Conesa, J. C.; Munuera, G. Interfacial redox processes under CO/O_2 in a nanoceria-supported copper oxide catalyst. *J. Phys. Chem. B* **2004**, *108*, 17983−17991.

(37) Pintar, A.; Batista, J.; Hocevar, S. TPR, TPO, and TPD examinations of $Cu_{0.15}Ce_{0.85}O_{2-y}$ mixed oxides prepared by co-precipitation, by the sol-gel peroxide route, and by citric acid-assisted synthesis. *J. Colloid Interface Sci.* **2005**, *285*, 218−231.

(38) Liu, Y.; Hayakawa, T.; Suzuki, K.; Hamakawa, S.; Tsunoda, T.; Ishii, T.; Kumagai, M. Highly active copper/ceria catalysts for steam reforming of methanol. *Appl. Catal., A* **2002**, *223*, 137−145.

(39) Huang, P.-X.; Wu, F.; Zhu, B.-L.; Gao, X.-P.; Zhu, H.-Y.; Yan, T.-Y.; Huang, W.-P.; Wu, S.-H.; Song, D.-Y. CeO_2 nanorods and gold nanocrystals supported on CeO_2 nanorods as catalyst. *J. Phys. Chem. B* **2005**, *109*, 19169−19174.

(40) Arango-Diaz, A.; Moretti, E.; Talon, A.; Storaro, L.; Lenarda, M.; Nunez, P.; Marrero-Jerez, J.; Jimenez-Jimenez, J.; Jimenez-Lopez, A.; Rodriguez-Castellon, E. Preferential CO oxidation (CO-PROX) catalyzed by CuO supported on nanocrystalline CeO_2 prepared by a freeze-drying method. *Appl. Catal., A* **2014**, *477*, 54−63.

(41) Du, L.; Wang, W.; Yan, H.; Wang, X.; Jin, Z.; Song, Q.; Si, R.; Jia, C. Copper-ceria sheets catalysts: Effect of copper species on catalytic activity in CO oxidation reaction. *J. Rare Earths* **2017**, *35*, 1186−1196.

(42) Lykaki, M.; Pachatouridou, E.; Carabineiro, S. A. C.; Iliopoulou, E.; Andriopoulou, C.; Kallithrakas-Kontos, N.; Boghosian, S.; Konsolakis, M. Ceria nanoparticles shape effects on the structural defects and surface chemistry: Implications in CO oxidation by Cu/CeO_2 catalysts. *Appl. Catal., B* **2018**, *230*, 18−28.

(43) Shaabani, B.; Alizadeh-Gheshlaghi, E.; Azizian-Kalandaragh, Y.; Khodayari, A. Preparation of CuO nanopowders and their catalytic activity in photodegradation of Rhodamine-B. *Adv. Powder Technol.* **2014**, *25*, 1043−1052.

(44) Wang, X.-Q.; Rodriguez, J. A.; Hanson, J. C.; Gamarra, D.; Martinez-Arias, A.; Fernandez-Garcia, M. Unusual physical and chemical properties of cu in $Ce_{1-x}Cu_xO_2$ oxides. *J. Phys. Chem. B* **2005**, *109*, 19595−19603.

(45) Lopez Camara, A.; Cortes Corberan, V.; Barrio, L.; Zhou, G.; Si, R.; Hanson, J. C.; Monte, M.; Conesa, J. C.; Rodriguez, J. A.; Martinez-Arias, A. Improving the CO-PROX Performance of Inverse CeO_2/CuO Catalysts: Doping of the CuO Component with Zn. *J. Phys. Chem. C* **2014**, *118*, 9030−9041.